



Article

# Continuous Eddy Simulation (CES) of Transonic Shock-Induced Flow Separation

Adeyemi Fagbade D and Stefan Heinz \*D

Department of Mathematics and Statistics, University of Wyoming, Laramie, WY 82071, USA; afagbade@uwyo.edu

\* Correspondence: heinz@uwyo.edu

Abstract: Reynolds-averaged Navier–Stokes (RANS), large eddy simulation (LES), and hybrid RANS-LES, first of all wall-modeled LES (WMLES) and detached eddy simulation (DES) methods, are regularly applied for wall-bounded turbulent flow simulations. Their characteristic advantages and disadvantages are well known: significant challenges arise from simulation performance, computational cost, and functionality issues. This paper describes the application of a new simulation approach: continuous eddy simulation (CES). CES is based on exact mathematics, and it is a minimal error method. Its functionality is different from currently applied simulation concepts. Knowledge of the actual amount of flow resolution enables the model to properly adjust to simulations by increasing or decreasing its contribution. The flow considered is a high Reynolds number complex flow, the Bachalo–Johnson axisymmetric transonic bump flow, which is often applied to evaluate the performance of turbulence models. A thorough analysis of simulation performance, computational cost, and functionality features of the CES model applied is presented in comparison with corresponding features of RANS, DES, WMLES, and wall-resolved LES (WRLES). We conclude that CES performs better than RANS, DES, WMLES, and even WRLES at a little fraction of computational cost applied for the latter methods. CES is independent of usual functionality requirements of other methods, which offers relevant additional advantages.

**Keywords:** computational fluid dynamics; large eddy simulation (LES); Reynolds-averaged Navier-Stokes (RANS) methods; hybrid RANS-LES methods



Citation: Fagbade, A.; Heinz, S. Continuous Eddy Simulation (CES) of Transonic Shock-Induced Flow Separation. *Appl. Sci.* **2024**, *14*, 2705. https://doi.org/10.3390/app14072705

Academic Editors: Paula Vasquez and Michael Cromer

Received: 20 February 2024 Revised: 12 March 2024 Accepted: 19 March 2024 Published: 23 March 2024



Copyright: © 2024 by the authors. Licensee MDPI, Basel, Switzerland. This article is an open access article distributed under the terms and conditions of the Creative Commons Attribution (CC BY) license (https://creativecommons.org/licenses/by/4.0/).

#### 1. Introduction

Accurate and feasible numerical simulations of turbulent flows are highly relevant. Such computational fluid dynamics (CFD) has impacted and transformed all aspects of human endeavor and industry [1]. CFD tools today are integral components of aerospace, defense, energy, power generation, transport, electronics, food processing, environmental management, fire safety, computational chemistry, particle physics, genetics, architecture and building design, and life, biomedical, and pharmaceutical sciences. The methodological basis of such simulations has hardly changed. The spectrum of usually applied methods ranges from non-resolving Reynolds-averaged Navier–Stokes (RANS) methods to resolving large eddy simulation (LES) [2–7], and in between such non-resolving and resolving methods we have hybrid RANS-LES methods [3,7–15].

In most applications of technical relevance, there is the need to simulate wall-bounded complex turbulent flows including separation. Such flow simulations suffer from well-known, basic problems for decades [7]. RANS simulations often provide unreliable results depending on the model applied. Wall-resolved LES (WRLES) suffers from significant, often unaffordable computational cost. Hybrid RANS-LES, usually detached eddy simulation (DES) methods [16–19], and wall-modeled LES (WMLES) [20–22], provide predictions that are significantly influenced by model setting options and (for the same number of grid points) the mesh distribution applied. Such issues can be seen in several areas, as for example aerospace, mesoscale, and microscale modeling in regard to atmospheric simulations, and many technical applications [7,23,24].

Current developments driven by several communities focus on exploring options to improve DES and WMLES methods.

There are novel methodological developments in this regard, such as minimal error simulation methods referred to as continuous eddy simulation (CES) [7,25–32]. Such CES methods can be used in conjunction with all usually applied turbulence models, including probability density function (PDF) and Reynolds stress equation methods. These methods are based on exact mathematics. They are essentially independent from a variety of simulation settings applied in WMLES and DES methods. Their use continuously enables simulations of partially resolving flow regimes ranging from RANS to LES. Such CES methods receive limited attention so far because their design is different from mainstream approaches. Unsteady RANS equations are known to be capable of involving resolved motion in simulations, but (similar to LES applied on coarse grids) this is no guarantee of a proper simulation performance. The idea that RANS-type equations can stably resolve flow like LES is not generally accepted. CES methods do not explicitly involve information about the grid as given by the filter width  $\Delta$ . The latter is usually seen as requirement for proper LES.

The motivation of this paper is to contribute to the clarification of the latter essential questions. The flow considered, which is the axisymmetric transonic bump flow experimentally studied by Bachalo and Johnson [33], is a complex and high Reynolds number (*Re*) flow. It stands as a well-established test case for assessing turbulence models due to its characteristics involving separation, shock waves, and downstream reattachment, along with various regions of steep gradients. Remarkably, this flow closely resembles the flow over an aircraft, such as the NASA Common Research Model (CRM) under transonic cruise conditions. RANS predictions of this flow reveal significant problems, i.e., the performance of simulation methods depends essentially on the proper inclusion of resolved motion. However, partially resolving simulation methods (such as DES and WMLES) and even WRLES face significant issues regarding such flow simulations. For example, Spalart et al. concluded that "WMLES results are disappointing, even in terms of the shock position, even though the results from two grids, respectively, agree well with each other. This failure of grid refinement to warn of an inaccurate simulation is of great concern" [34].

The following are the specific objectives of our investigation:

- O1. Performance features: demonstration that CES methods are characterized by a simulation performance that is better than the performance of RANS and usually applied hybrid RANS-LES (in particular DES and WMLES methods) and at least as good as the performance of WRLES.
- O2. Cost features: demonstration that the computational cost of CES is significantly below the cost of hybrid RANS-LES (DES and WMLES methods) and WRLES.
- O3. Functionality features: Demonstration that CES is independent of significant functionality requirements of hybrid RANS-LES and WRLES (choice of sufficiently fine grids, appropriate mesh distributions, specific simulation settings for a flow considered, validation data needed to determine simulation settings).

This paper is organized in the following way. Section 2 introduces the modeling and computational approach. Section 3 describes the resolution features of the CES model considered. Section 4 compares the performance and computational cost of CES with RANS, DES, WMLES, and WRLES methods. The conclusions of this study are presented in Section 5.

### 2. Modeling and Computational Approach

# 2.1. Modeling Approach

The motivation of the modeling approach is to cover both RANS and LES regimes via the implementation of a flow-resolving capability in RANS equations, with the understanding that the use of this model in resolving mode is equivalent to the use of LES. On the one hand, the implementation in RANS equations ensures a model complexity usually applied in RANS approaches. On the other hand, this approach avoids the typical LES problem given

Appl. Sci. 2024, 14, 2705 3 of 22

by the use of an artificial (i.e., non-physical) length scale (the filter width  $\Delta$ ) [35]. The latter is the reason for significant LES problems: the need to use very fine grids (which implies very high computational cost) to ensure accurate results, and (very often) uncertainty regarding how well resolving a particular LES actually is. The hybridization approach applied (the set up of continuous eddy simulation (CES) methods [7,25–32]) can be used in conjunction with a variety of turbulence models, including probability density function (PDF) and Reynolds stress equation methods [7,30,36]. In an attempt to focus on the main advantages of this approach, it will be applied here on the level of two-equation eddy viscosity methods. The essential steps of the modeling approach will be described in the following paragraphs focusing on the equations considered, the hybridization approach, and the model functioning.

We consider the compressible continuity equation and momentum equation [28],

$$\frac{\widetilde{D}\widetilde{\rho}}{\widetilde{D}t} = -\widetilde{\rho}\frac{\partial\widetilde{U}_k}{\partial x_k}, \qquad \frac{\widetilde{D}\widetilde{U}_i}{\widetilde{D}t} = -\frac{1}{\widetilde{\rho}}\frac{\partial\widetilde{\rho}}{\partial x_i} + \frac{2}{\widetilde{\rho}}\frac{\partial(\widetilde{\rho}v\widetilde{S}_{ij}^d)}{\partial x_j} - \frac{1}{\widetilde{\rho}}\frac{\partial(\widetilde{\rho}\tau_{ij})}{\partial x_j}.$$
(1)

The tilde refers to space-averaged variables, and  $\widetilde{D}/\widetilde{D}t=\partial/\partial t+\widetilde{U}_j\partial/\partial x_j$  represents the filtered Lagrangian time derivative. Components of the velocity vector are denoted by  $\widetilde{U}_i$ , and  $\widetilde{p}$ ,  $\widetilde{\rho}$ , and  $\nu$ , represent pressure, fluid density, and kinematic viscosity, respectively. The rate-of-strain tensor reads  $\widetilde{S}_{ij}=(\partial\widetilde{U}_i/\partial x_j+\partial\widetilde{U}_j/\partial x_i)/2$ , and its deviatoric part is given by  $\widetilde{S}_{ij}^d=\widetilde{S}_{ij}-\widetilde{S}_{nn}\delta_{ij}/3$ . Throughout this paper, we use the sum notation. The right-hand side (RHS) of the momentum equation contains an unknown, the modeled stress tensor  $\tau_{ij}$ . The eddy viscosity model assumes for this stress  $\tau_{ij}=2k\delta_{ij}/3-2\nu_t\widetilde{S}_{ij}^d$ . Here,  $\delta_{ij}$  is the Kronecker delta, k represents the modeled kinetic energy, and  $\nu_t=C_\mu k/\omega$  is the turbulent viscosity of the flow which includes the turbulence frequency  $\omega=1/\tau$  and the model parameter  $C_\mu$  having a standard value  $C_\mu=0.09$ . Here, the turbulence time scale  $\tau=k/\varepsilon$  is related to k and the dissipation rate  $\varepsilon$ .

The model viscosity  $v_t$  is closed via a two-equation turbulence model, in particular a  $k - \omega$  model that provides k and  $\omega$  for  $v_t = C_u k / \omega$ . We consider the equations [37]

$$\frac{\widetilde{D}k}{\widetilde{D}t} = P - \epsilon + D_k, \qquad \frac{\widetilde{D}\omega}{\widetilde{D}t} = C_{\omega_1}\omega^2 \left(\frac{P}{\epsilon} - \beta\right) + D_\omega + D_{\omega c}. \tag{2}$$

Here, turbulence production is given by  $P = \nu_t S^2$  (which involves the strain rate  $S = (2\widetilde{S}_{mn}^d \widetilde{S}_{nm}^d)^{1/2}$ ), the dissipation of k is given by  $\epsilon = k\omega$ , and  $\beta = C_{\omega_2}/(C_k C_{\omega_1})$ . The diffusion terms involved read

$$D_{k} = \frac{\partial}{\partial x_{j}} \left[ \left( \nu + \nu_{t} \right) \frac{\partial k}{\partial x_{j}} \right], \quad D_{\omega} = \frac{\partial}{\partial x_{j}} \left[ \left( \nu + \frac{\nu_{t}}{\sigma_{\omega}} \right) \frac{\partial \omega}{\partial x_{j}} \right], \quad D_{\omega c} = \frac{C_{\omega}}{k} (\nu + \nu_{t}) \frac{\partial k}{\partial x_{j}} \frac{\partial \omega}{\partial x_{j}} \quad (3)$$

The model parameters involved have the values

$$C_{\omega 1} = 0.49$$
,  $C_{\omega 2} = 0.072$ ,  $C_{\omega} = 1.1$ ,  $C_k = 0.09$ ,  $\sigma_{\omega} = 1.8$ .

The cross-diffusion term  $D_{wc}$  is added to  $D_w$ , although its relevance is subject to questions (it is supposed to reduce the inaccurate behavior of  $k-\omega$  models for free shear layer flow simulations) [38]. Numerical errors induced by the integration of the  $\omega$  equation across the viscous sub-layer can compromise the accurate simulation of the velocity profile [39]. To circumvent this problem,  $\omega = 2v/d^2$  is applied to specifically set the value of  $\omega$  at the first cells above the wall, while d accounts for the distance between the wall and the center of the first cell. We note that the expression  $\omega = 2v/d^2$  is derived under the assumption that the first cell center lies within the viscous sub-layer, alternative settings of which are available in [38].

Appl. Sci. 2024, 14, 2705 4 of 22

The hybridization can be accomplished in several ways [27]. By following our recent approach [25], we address the hybridization by a modification of the dissipation in the scale equation by the introduction of an unknown function  $\beta^*$ , which replaces  $\beta$  in Equation (2),

$$\frac{\widetilde{D}k}{\widetilde{D}t} = P - \epsilon + D_k, \qquad \frac{\widetilde{D}\omega}{\widetilde{D}t} = C_{\omega_1}\omega^2 \left(\frac{P}{\epsilon} - \beta^*\right) + D_\omega + D_{\omega c}. \tag{4}$$

We refer to the model described in the following as CES-KOS (or simply KOS), where KO refers to the use of an  $k-\omega$  model and KOS refers to a hybridization of the scale equation. Essential steps of the hybridization described elsewhere [27] are the following ones. The production term in the  $\omega$  equation is replaced by using the k equation and the first variation in the resulting  $\omega$  equation is considered. The hybridization error becomes minimal for a zero first-order variation. The latter provides a relationship between variations of model parameters ( $\beta^*$ ) and model variables (like k and  $\omega$ ). The integration of this relationship from a complete modeling state to a state of partial modeling implies

$$\beta^* = 1 + R(\beta - 1). \tag{5}$$

Here, R (which characterizes the flow resolution degree) will be discussed in the next paragraph. In order to obtain  $\beta^* = 1 + R(\beta - 1)$ , we neglected for simplicity  $D_{\omega c}$  and the substantial derivatives  $\widetilde{D}k/\widetilde{D}t$  and  $\widetilde{D}\varepsilon/\widetilde{D}t$ . It is possible to involve the latter terms at the cost of more complex equations [29]. Relevant assumptions also made to obtain  $\beta^* = 1 + R(\beta - 1)$  are normalized first variations  $\delta k/k$  and  $\delta \omega/\omega$  which are invariant in space and time. It is worth noting that the latter assumptions do not involve any restriction of the modeling approach, as these assumptions stabilize the flow resolution in space and time. These equations were applied in conjunction with the elliptic blending approach used in our previous work to account for wall damping [40] (in the RANS-mode for all the flow fields).

The model functioning is essentially related to the variable R. The hybridization approach provides the relation  $R=L_{+}^{2}$ . Here,  $L=k^{3/2}/\epsilon$  refers to the length scale of modeled motions, and  $L_{+} = L/L_{tot}$  is the turbulence length scale resolution ratio incorporating both modeled (L) and total contributions ( $L_{tot}$ ) [7]. The modeled contribution is calculated by  $L = \langle k \rangle^{3/2} / \langle \epsilon \rangle$ . The brackets refer to averaging in time. The total length scale is calculated correspondingly by  $L_{tot} = k_{tot}^{3/2}/\epsilon_{tot}$ . In these relations, we have  $k_{tot} = \langle k \rangle + k_{res}$ , where  $k_{res} = (\langle \tilde{U}_i \tilde{U}_i \rangle - \langle \tilde{U}_i \rangle \langle \tilde{U}_i \rangle)/2$ . Correspondingly,  $\epsilon_{tot}$  is the sum of modeled and resolved contributions,  $\epsilon_{tot} = \langle \epsilon \rangle + \epsilon_{res}$ . Here, the resolved contribution is calculated by  $\epsilon_{res} = \nu \left( \left\langle \partial U_i / \partial x_j \partial U_i / \partial x_j \right\rangle - \left\langle \partial U_i / \partial x_j \right\rangle \left\langle \partial U_i / \partial x_j \right\rangle \right)$ . The differences between the concept described here and related partially averaged Navier-Stokes (PANS) and partially integrated transport (PITM) models are discussed elsewhere [7,31]. First of all, these differences are seen in regard to the ability of models to accomplish a desired imposed flow resolution. In particular, PANS and PITM approaches suffer from discrepancies between the imposed and actual flow resolution, which may imply significant deficiencies of the simulation performance of PANS and PITM methods. It is worth noting, however, that  $\epsilon_+ = \epsilon/\epsilon_{tot}$  is usually found to be well-approximated by unity except very close to walls. If this approximation is applicable, it implies that  $R = L_{+}^{2} = k_{+}^{3}$ .

The involvement of R in the model via  $\beta^* = 1 + R(\beta - 1)$  characterizes an essential difference to usually applied modeling approaches focusing on imposing a certain desired flow resolution via the model set up. Within the CES-KOS modeling approach, the model is informed about the actual flow resolution via R. This enables the model to properly respond to changes in the amount of resolved motion (implied by changes in the mesh density or different Re). In particular, the model contribution can decrease (increase) if there is a significant amount of (little) resolved motion. Without implementation of this mechanism, the model cannot properly transition between LES and RANS regimes characterized by a significant amount of (no) resolved motion.

Appl. Sci. 2024, 14, 2705 5 of 22

### 2.2. Flow Considered

Figure 1 shows a schematic diagram of the experimental configuration and the computational domain for the axisymmetric transonic bump considered along with the applied boundary conditions. This case pertains to shock-triggered boundary layer separation induced by an axially symmetric bump mounted on a slim spherical cylinder, which extends 61 cm upstream. The case reflects the upper surface of a transonic wing. It is characterized by a Mach number ( $M_{\infty}$ ) of 0.875 and a Reynolds number (Re) of 2.763 M relative to the airfoil's chord length c. Main flow features are also shown in Figure 2.

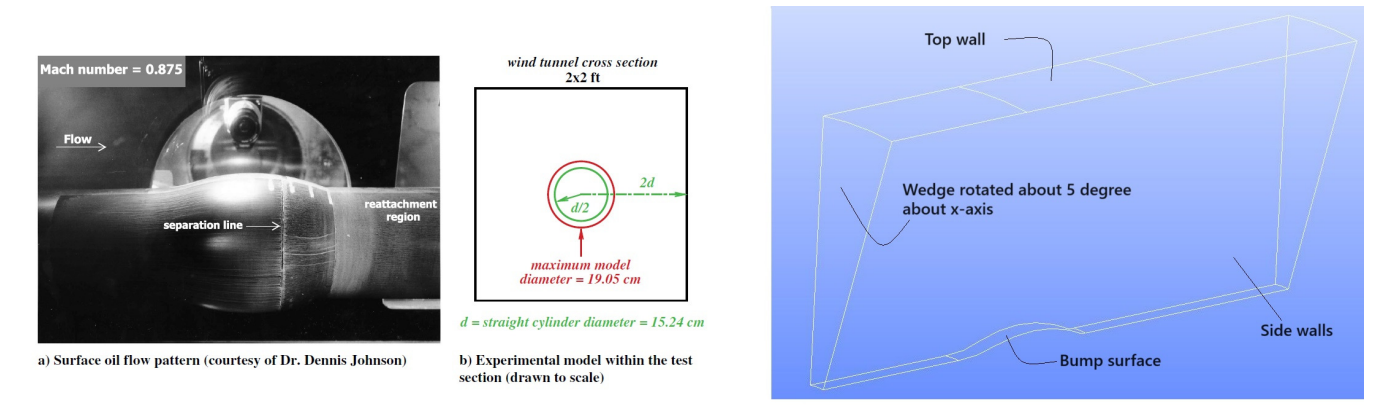


Figure 1. Axisymmetric transonic bump geometry: Experimental and computational configuration [41,42].

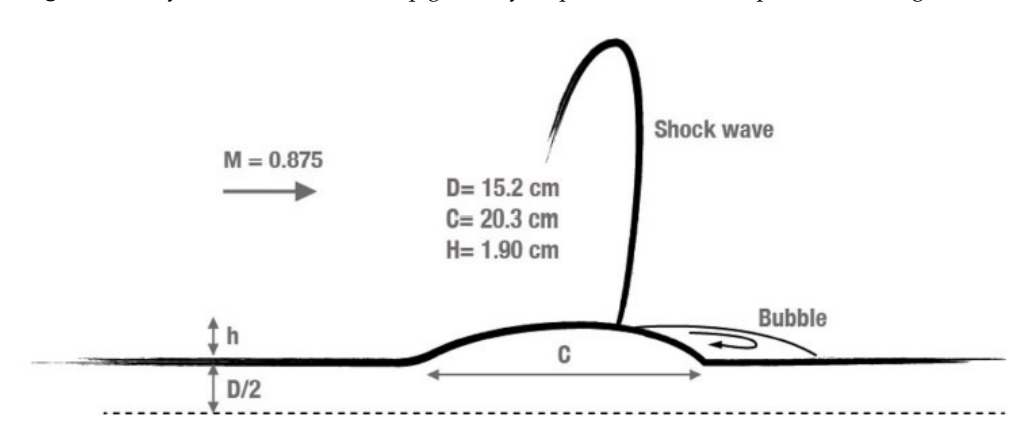


Figure 2. Main flow features [43].

The experiment [33] was conducted using a closed return tunnel with a variable density and featured a spherical cylindrical body with a diameter of 0.152 m. The tunnel had upper and lower walls, both made up of porous-slotted material, which allowed approximately 21% of open area. The incident boundary layer on the bump measured approximately 1 cm in thickness, and the estimated momentum-thickness Reynolds number at a point of 1.5 chord lengths was around  $Re_{\theta} \approx 6600$ . The chord length of the bump was fixed at 0.2032 m. In the experiment, a shockwave formed downstream of the bump, which extended from the cylindrical surface. This shockwave, along with an adverse pressure gradient, led to unsteady flow separation from the surface with reattachment further downstream. The reattachment point is largely influenced by the turbulent stresses generated in the detached shear layer.

While the Bachalo–Johnson [33] experiment has provided detailed data on mean velocity profiles, the Reynolds shear stress, and surface pressure, it is important to note that measurements of skin friction coefficients were omitted. The latter were provided by a recent experiment of Lynch et al. [44].

## 2.3. Computational Approach

Given the axisymmetric nature of the test case, we designed the computational domain as a slender wedge with an angle  $\leq 5^{\circ}$  and a single cell thickness along the plane of symmetry. This setup process is documented in [45] and illustrated in Figure 1. The domain's length extended to 7.63 D (see Figure 2), while the height of the wedge matched 3.62 D. The spherical bump geometry starts at x/c = 0, with the inlet patch located at x/c = -1.5 and the exit boundary at x/c = 4.4 in the main geometry. The relevant physical domain extends to x/c = 2. To construct a block-structured grid suitable for the bump domain, we employed Salome in conjunction with the snappyHexMesh mesh generator provided by OpenFOAM. OpenFOAM has several solvers for both incompressible and compressible flows (e.g., SonicFOAM and RhoCentralFOAM, etc.). For the current work, we have applied an unstructured finite-volume solver, SonicFOAM, a transient solver for transonic/supersonic, laminar, or compressible flow. Two meshes,  $G_1$  and  $G_2$ , were created with different cell counts in the longitudinal and transverse directions, as shown in Figure 3. Detailed characteristics of these meshes are provided in Table 1. Both meshes used non-uniform grading, with cells stretched in the axial direction and compressed in the transverse direction, particularly near the wall and bump region. The mesh density was enhanced in the expected shock region. The initial cell dimension near the surface was set to 1 mm for both meshes, resulting in a mean value of  $y^+$  of 30. Using an axisymmetric grid, we simulate in this way a slice of the 3D axisymmetric bump geometry (a spanwise-periodic configuration with the same cross-sectional profile as given by the three-dimensional bump geometry). The same approach was applied by Ren et al. [41] as well as Elnahhas et al. [46].

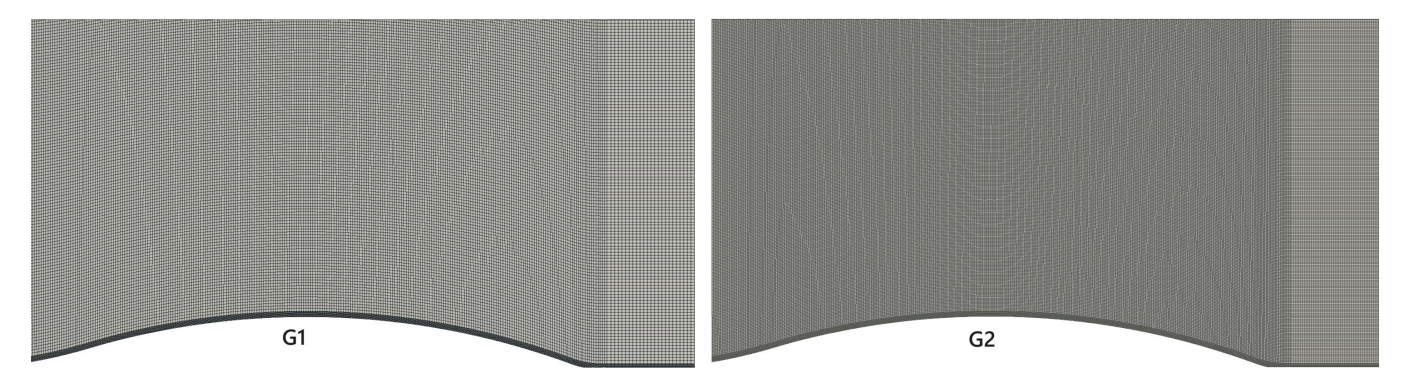


**Figure 3.** Partial view of the grids applied for the bump case: coarse grid  $G_1[300 \times 120]$ , fine grid  $G_2[600 \times 150]$ .

	<b>Table 1.</b> The grids	applied and s	specifications of the	simulation parameters.
--	---------------------------	---------------	-----------------------	------------------------

Run	Grid	$N_{cells}$	$N_x \times N_y \times N_z$	Min. Wall Spacing	$\Delta y^+$
$G_1$ $G_2$	Coarse Fine	1.08 M 5.4 M	$300 \times 120 \times 30$ $600 \times 150 \times 60$	0.00001 0.000001	1.00 0.85
Reynolds numbers	Mach number	Char. length	Spatial domain		
Re = (2.763  M, 5.5  M)	0.875	c = 0.2032  m	$7.63 \mathrm{~D} \times 3.62 \mathrm{~D} \times 5^{\circ}$		

Characteristic boundary conditions were imposed at the freestream and outflow boundaries. Efficiently characterizing turbulent inflow conditions remains a persistent challenge for hybrid simulations. A precursor RANS simulation utilizing the k- $\omega$  model was employed. This involved extracting mean velocity and other data (see Figure 4) from the mapping plane to provide a proper turbulent inflow at x/c = -1. The set-up involved a composite setting at the inlet boundary. Specifically, velocities within the turbulent boundary layer were directly mapped at a predefined distance downstream,

Appl. Sci. 2024, 14, 2705 7 of 22

while upper-wall velocities were set to a fixed value, as depicted in Figure 4. The computed total mass flow rate in conjunction with the turbulent viscosity profile established a comprehensive inflow profile. The lateral surfaces, on the other hand, employed a wedge boundary condition, which enforces equal and opposite fluxes on both sides. The bump's surface is subjected to a solid wall boundary condition. At the outlet, zero gradients were applied for velocities and turbulent stresses. Since the flow is compressible, an appropriate characteristic-based or pressure-outlet condition was applied at the outlet. The latter allowed for the reflection of pressure waves, including shock waves.

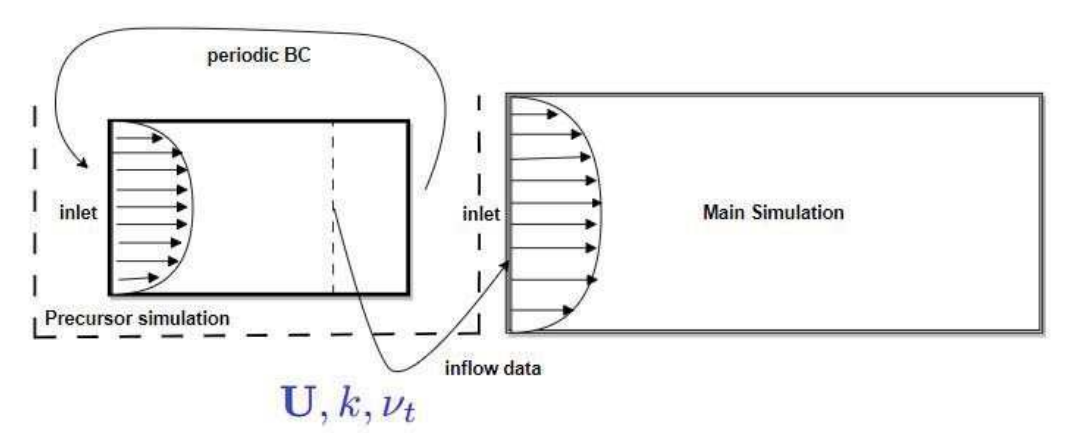


Figure 4. Illustration of inflow simulation.

The initial time-step of the simulation was set at  $10^{-3}c/U_{\infty}$  for the  $G_1$  grid, ensuring a consistent CFL number of 0.4 in all simulations. The total sampling time of the CES-KOS simulation on both grids was 14 convective units  $(c/U_{\infty})$ . Nine (9) of these units were utilized to achieve a steady state of the simulation, while the remaining five (5) units were dedicated to the collection of turbulence statistics. Due to the interaction between the shock and turbulent boundary layer, the flow separates over the bump, and subsequently reattaches at a location further downstream on the cylinder surface [43]. Figure 2 illustrates the characteristic shock wave and the flow detachment following the shock on the bump. To numerically solve the discretized equations, we used an algebraic multi-grid solver with the van Leer scheme. The latter is a second-order upwind-based discretization scheme. The solution was considered to be converged when the relative error magnitudes of the computed flow variables reached  $10^{-6}$ . The flow dynamics and corresponding shock-wave interactions were studied at two main Reynolds numbers: Re = (2.763 M,5.5 M). Measurements for comparison are only available for the Re = 2.763 M case. The grid and Re variations in our simulations cover resolutions ranging from well-resolved LES to almost RANS modeling. In particular, the Re = 2.763 M ( $G_2$  case) approximates a well-resolved LES, and the Re = 5.5 M ( $G_1$  case) represents RANS-type modeling. By covering LES to RANS regimes, our simulations enable the investigation of resolution effects on separation predictions.

# 3. CES-KOS Resolution Features

# 3.1. Resolution Features

Characteristic resolution features of the CES-KOS model will be illustrated first. Figure 5 and Table 2 show velocity fluctuations (u and v) for different Re and resolution conditions, in particular the Re = 5.5 M ( $G_2$ ,  $G_1$ ) and Re = 2.763 M ( $G_2$ ,  $G_1$ ) cases. These cases cover a range of flow resolution conditions, from nearly fully resolved (Re = 2.763 M,  $G_2$ ) to predominantly RANS-type (Re = 5.5 M,  $G_1$ ) conditions. The Re = 2.763 M( $G_2$ ) case shows a diverse range of small-scale vortices within the recirculation region, indicating a high level of flow resolution. On the other hand, the Re = 5 M ( $G_1$ ) case exhibits an unsteady RANS-type regime, in which fluctuations persist, but small-scale turbulence structures are hardly resolved anymore. The transitional cases (Re = 2.763 M ( $G_1$ ) and

 $Re = 5.5 \,\mathrm{M}$  ( $G_3$ )) show less fine-scale structures than the ( $Re = 2.763 \,\mathrm{M}$ ,  $G_2$ ) case due to the grid coarsening and increased Re, respectively. Specific observations are the following ones: (i) Grid coarsening and higher Re cause continuous changes of fluctuations, without sudden shifts. The most noticeable change is the spatial clustering of fluctuations, while the overall strength of fluctuations remains largely unaffected. (ii) In particular, under unstationary RANS conditions, fluctuations are still present (they do not disappear). It is interesting to see that the strength of fluctuations is comparable to the strength of fluctuations under resolving conditions.

**Table 2.** Range of velocity fluctuations for the cases described in Figure 5.

Fluc.	y/c=0.48	y/c = 0.6	y/c = 0.8
и	$-0.002 \le u \le 0.002$	$-0.003 \le u \le 0.003$	$0.004 \le u \le 0.004$
v	$-0.003 \le v \le 0.003$	$-0.004 \le v \le 0.004$	$0.004 \le v \le 0.004$

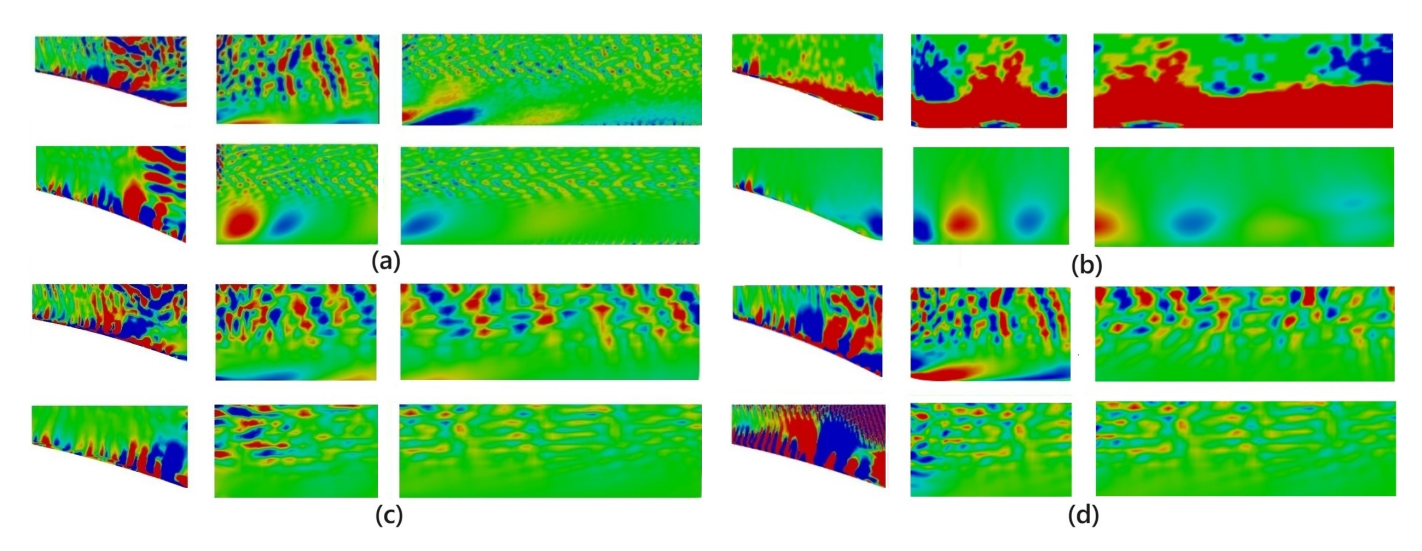


**Figure 5.** Velocity fluctuations u, v (top to bottom) within and off the recirculation region in xz planes at y = (0.48, 0.6, 0.8)c (left to right) for (a) Re = 5.5 M (G2), (b) Re = 5.5 M (G1), (c) Re = 2.763 M (G2), (d) Re = 2.763 M (G1) cases. The color scale is given in Table 2. Positive (negative) fluctuations are represented by red (blue) regions.

Figure 6 shows local resolution characteristics of the CES-KOS model, specifically  $L_+ = L/L_{tot}$ ,  $k_+ = k/k_{tot}$ , and  $\epsilon_+ = \epsilon/\epsilon_{tot}$  for different grids at different positions. Apart from looking at specifics, the  $k_+$  profile, for example, shows significant changes in the flow resolution ranging from almost RANS regimes close to the walls to (depending on the grid) resolving regimes in the core of the flow. It is essential to note that these resolution variations take place smoothly; there are no oscillations in the resolution indicators. The latter is a consequence of the model set-up assuming, for example, spatially invariant variational contributions  $\delta k/k$ . The grid effect is as required: the use of a finer grid implies more resolution, which decreases  $L_+ = L/L_{tot}$  and  $k_+ = k/k_{tot}$ . As observed also otherwise [25],  $\epsilon_+$  values were found close to unity, but grid effects are clearly present.

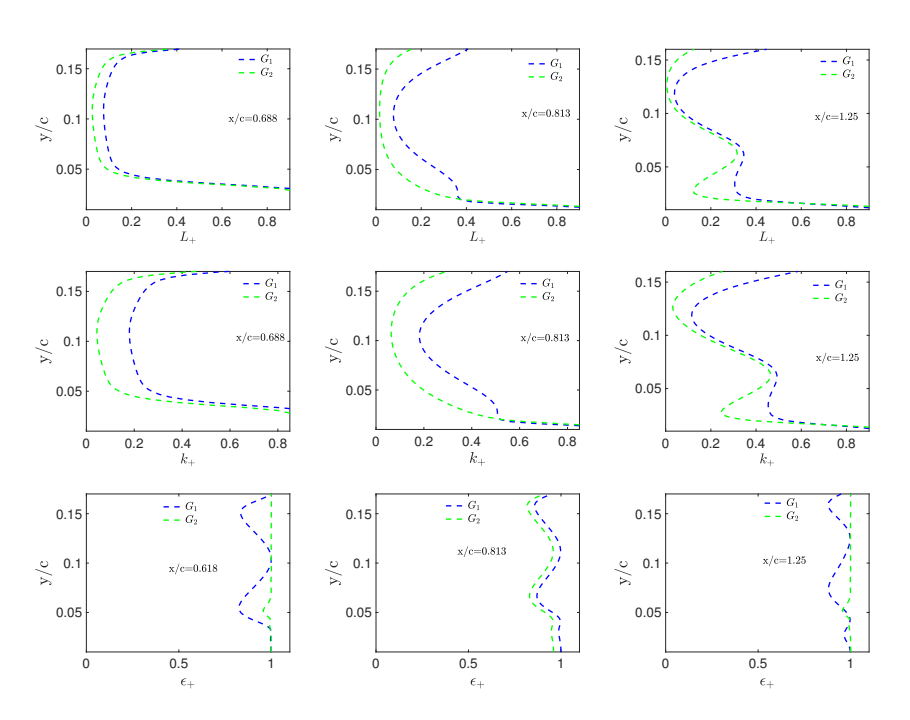


**Figure 6.** CES-KOS flow resolution features: L+, k+, and  $\epsilon_+$  (first, second, and third row) are shown at the given x/c.

## 3.2. Flow Simulations: Grid Effects

Figure 7 shows the spatial distribution of fluctuations, velocity magnitude, and pressure. A  $\lambda$ -structure-like shock pattern is seen over the bump region in particular in pressure and velocity contour plots. The pressure contour shows a diminishing pressure within the shock region compared to the downstream distribution. The interplay between the impinging shock wave and boundary layer triggers the downstream boundary layer propagation and leads to an unsteady separation bubble formation near the trailing edge.

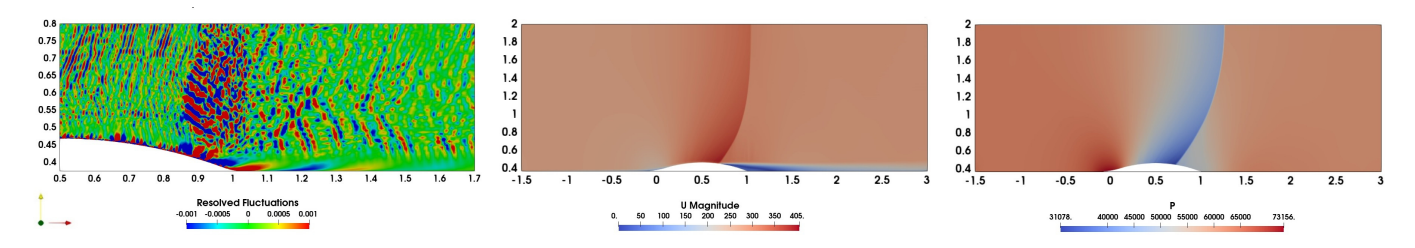
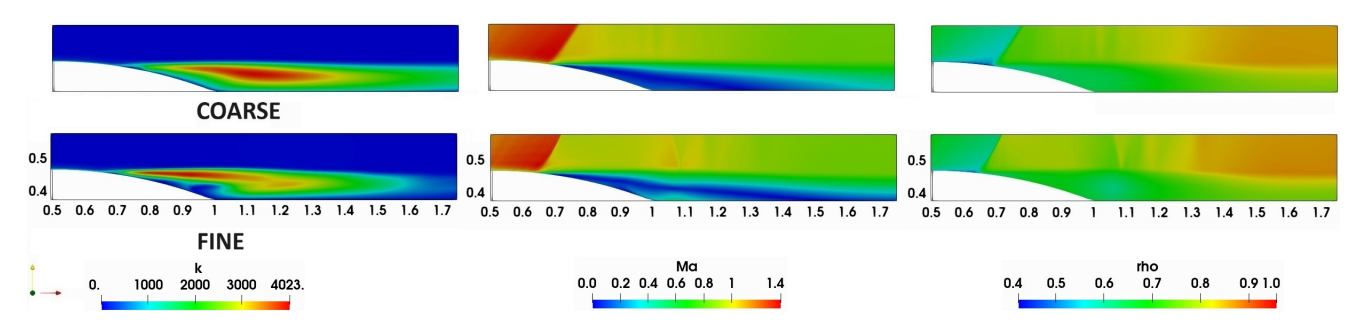


**Figure 7.** CES-KOS simulations on  $G_2$ : contour plots of fluctuations, velocity magnitude, and pressure.

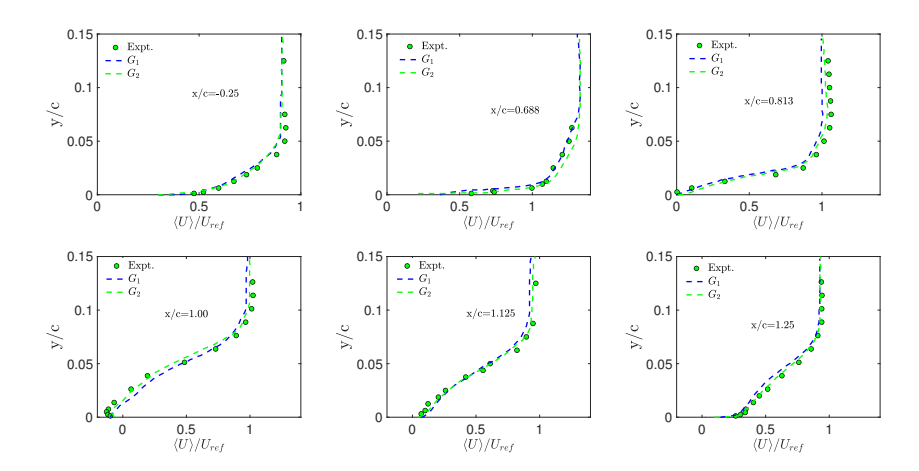
Figure 8 shows corresponding modeled kinetic energy k, Mach number, and density variation for the two grids applied. The shock structure can be clearly seen in the Mach number and density distributions. Both grids predict a Mach number up to 1.4 prior to flow separation. The modeled kinetic energy k is particularly large in the separation and post-separation regions. The fine grid producing more flow resolution provides slightly smaller values of the modeled kinetic energy k and correspondingly more pronounced fine-scale structures.

In Figure 9, we compare CES-KOS predictions of mean velocities with experimental data at six locations: the equilibrium region (at x/c = -0.25), near separation (x/c = 0.688), within the separation region (x/c = 0.813), close to reattachment (x/c = 1.00, 1.125), and in the recovery region (x/c = 1.25). Overall, there is an excellent agreement between CES-KOS predictions on both grids applied and experimental data: minor improvements can be seen if the finer  $G_2$  grid is implied. An almost perfect agreement of simulations and

measurements is found at x/c = -0.25. At x/c = 0.688, which is in the region after the shock location but prior to detachment, there are noticeable but small deviations in the  $G_2$  grid results close to the boundary layer margins and away from the wall. However, at positions x/c = (0.813, 1.0, 1.125), which fall within the separation zone, the predictions align well with the measurements. Beyond the separation zone at x/c = 1.25, following the flow reattachment, there is again an excellent agreement. Overall, the predictions are in very good agreement with measurements, comparable to results in Mor-Yossef's work [47], which applies low-diffusion AUFSR schemes.

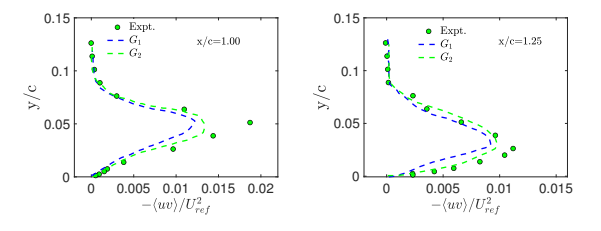


**Figure 8.** CES-KOS simulations: contour plots of modeled kinetic energy k, Mach number, and density on  $G_1$  (**first row**) and  $G_2$  (**second row**).



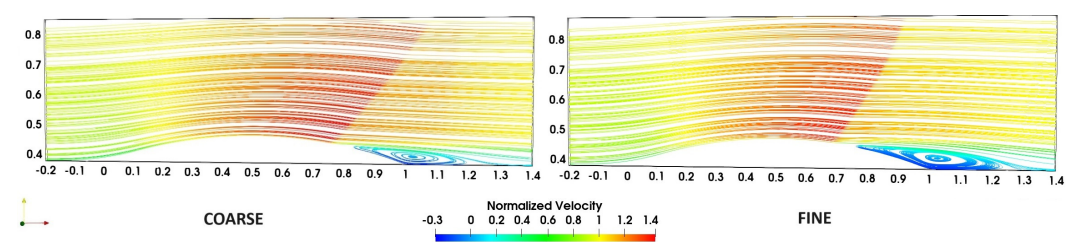
**Figure 9.** CES-KOS simulations: profiles of the normalized streamwise velocity  $\langle U \rangle / U_{ref}$  at different axial locations for the two grids applied.

The Reynolds-stress profiles presented in Figure 10 show minor discrepancies between the simulated and measured stresses. Close to the reattachment location at x/c = 1.00, the simulated stresses are lower than the measured stresses near the wall, with a maximum difference of 31% near the peak of the bump. At x/c = 1.25 in the post-reattachment region, the simulated Reynolds stress profile closely matches the experimental profile in the far field. It is worth noting that the  $G_1$  grid results deviate somewhat more from the measurements compared to the  $G_2$  grid profile, indicating the relevance of grid refinements.



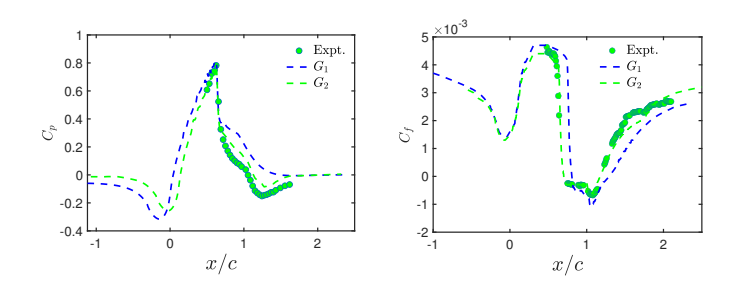
**Figure 10.** CES-KOS simulations: profiles of the normalized Reynolds stress  $\langle uv \rangle / U_{ref}^2$  at different axial locations for the two grids applied.

Figure 11 shows flow streamlines colored by mean velocity magnitude for the two grids applied. The shock-wave line is clearly visible. The plot shows a noticeable difference between the streamlines of grid  $G_1$  and  $G_2$ : the  $G_2$  result shows a considerably larger separation bubble. Notably, the finer CES-KOS grid result aligns more closely with DNS streamlines (see Figure 10 in Ref. [34]), although this is not displayed here. The figure relates to the detachment and reattachment points reported in Table 3 in comparison with measurements [33]. Despite small discrepancies in the exact locations of separation and reattachment, the  $G_2$  prediction shows better correspondence to the shock location obtained experimentally than the  $G_1$  result. The CES-KOS model characterizes the reattachment location slightly downstream due to relatively long separation bubble length.



**Figure 11.** Time-averaged streamline across the flow domain colored by mean velocity magnitude:  $G_1$  case **left**,  $G_2$  case **right**.

Figure 12 shows pressure  $(C_p)$  and skin friction  $(C_f)$  predictions. For a more detailed discussion of grid effects, we consider four sub-regions of the domain. The initial region extends from  $-1.0 \le x/c < 0.2$ , capturing a turbulent boundary layer with a pressure gradient transitioning from zero to adverse to favorable. The second region covers  $0.2 \le x/c < 0.6$ , incorporating the remaining favorable pressure gradient region and ending with the interaction between shock and boundary layer. The third region stretches from  $0.6 \le x/c < 1.25$ , which covers the separation bubble. Lastly, the fourth region covers the reattachment region,  $1.25 \le x/c \le 2.5$ . The  $C_p$  profiles show a clear grid dependence (with significant variations) in the first and second regions, whereas the  $C_f$  profiles are nearly grid-independent. Specifically, the G<sub>2</sub> simulation accurately captures the elbow-like feature in the pressure distribution at  $x/c \approx 1.15$  caused by the bump's slope change; the  $G_1$  grid simulation fails to replicate this feature. There is a slight overestimation of the  $C_f$ peak in the third region, with refinement leading to a monotonic decrease closer to the measurements. Refinement also improves the predicted shock location upstream, aligning better with the experiment (see Table 3). In post-shock regions, while surface pressure agrees satisfactorily overall, separation and reattachment points differ slightly between simulations and the measurement. For instance, in the  $0.6 \le x/c < 1.25$  region, separation occurs at x/c = 0.8338 ( $G_1$ ) and x/c = 0.7030 ( $G_2$ ), with predictive error margins of 4–22%. The  $G_2$  reattachment point (x/c = 1.1188) matches the measured x/c = 1.1000 [33] better than the  $G_1$  estimation (x/c = 1.1479).



**Figure 12.** CES-KOS simulations: profiles of pressure and skin-friction coefficients for the two grids applied.

Cases	Re	Separation Location (x/c)	Reattachment Location $(x/c)$	Bubble Length $\Delta x/c$	Error in Bubble Length Prediction (%)
Expt. [33] $G_1$ $G_2$	2.763 M 2.763 M 2.763 M	0.70 0.8338 0.703	1.10 1.1479 1.1188	0.4 0.3141 0.4158	21.5 3.95
G <sub>2</sub>	5.5 M	0.7105	1.1652	0.4547	_

Table 3. CES-KOS separation and reattachment characteristics.

# 3.3. Flow Simulations: Reynolds Number Effects

The study of Re effects is certainly of interest, and the CES concept provides a much improved basis to address such questions than given by other modeling approaches (see introduction). Corresponding results of CES-KOS simulations will be reported here by expanding simulations of the Re = 2.763 M case to Re = 5.5 M simulations. A qualitative impression is provided by Figure 13, which shows streamline structures for the low- and high-Re regimes. Correspondingly, as Re is increased from Re = 2.763 to 5.5 M, a larger separation bubble is observed. Table 3 presents a summary of the variations of separation and reattachment points at different Re along with the experimental data. It may be seen that increasing Re causes an increasing size of the separation bubble. The difference of separation bubbles between Re = 2.673 M and Re = 5.5 M is less than 10%.

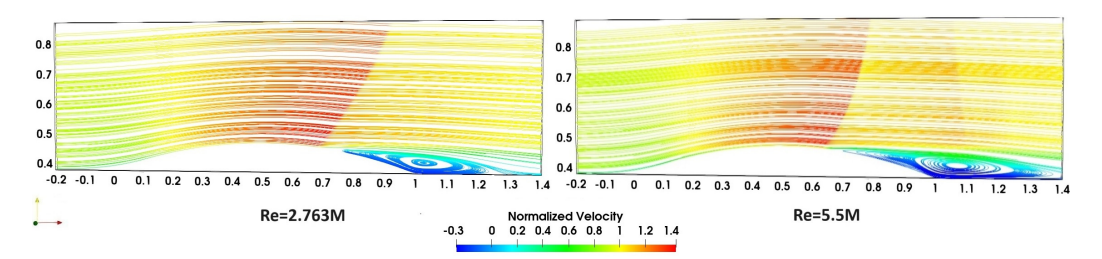


**Figure 13.** Time-averaged streamline across the flow domain colored by mean velocity magnitude: Re = 2.763 M case left, Re = 5.5 M case right.

Overall, Figure 14 shows that higher Re values have a minimal influence on the velocity profile of the flow [48]. In particular at x/c = 1.125 and 1.375, the boundary layer thickness near the lower wall seems to expand with increasing Re. Similar observations are made in regard to the Reynolds shear stress profile in the mid-separation region: there are only minor Re effects. Figure 14 also shows corresponding profiles of the pressure coefficient  $(C_p)$  and skin-friction coefficient  $(C_f)$ . It may be seen that the  $C_p$  profiles are hardly affected by Re effects. Although the separation locations for the two cases are not very different, the lower Re case indicates an earlier reattachment at  $x/c \approx 1.1188$ , while the reattachment occurs at approximately  $x/c \approx 1.1652$  for Re = 5.5 M (see Table 3). Prior to flow separation, the  $C_f$  peak is significantly higher in the Re = 5 M case than for the Re = 2.763 M case, indicating that the turbulence is highly intermittent in this zone. This finding aligns with the common understanding that higher Reynolds numbers correspond to increased skin friction, identified as the dominant drag in numerous practical applications. Orlü and Schlatter [49] attributed this effect to the growing influence of the large-scale turbulence structures, strong and accelerated flow over the bump and an implied impact on the wall-shear stress. These factors contribute to an amplified growth rate of the separated shear layer and consequently impact the reattachment location reported in Table 3.

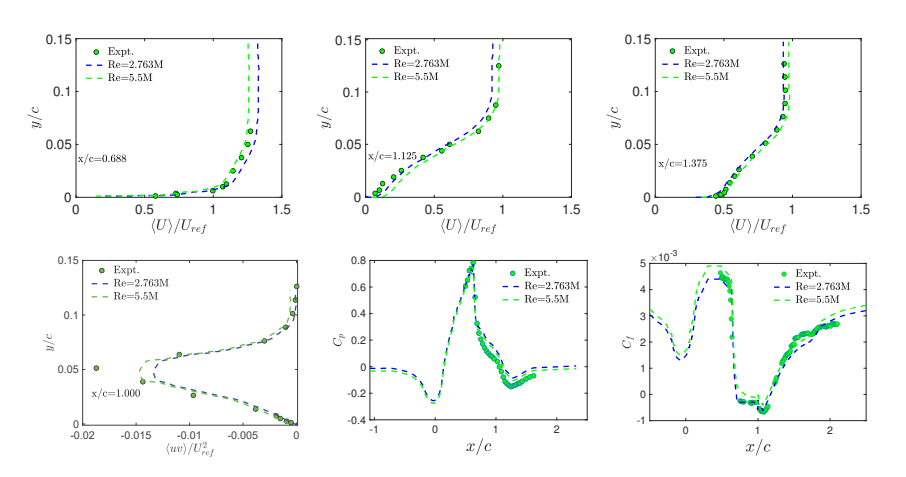


**Figure 14.** CES-KOS simulations: Re effect on profiles of the normalized streamwise velocity  $\langle U \rangle / U_{ref}$  and normalized Reynolds shear stress  $\langle uv \rangle / U_{ref}^2$  at different axial locations.

# 4. CES-KOS vs. RANS, DES, WMLES, and WRLES

The advantages of CES-KOS related to its ability to provide well-controlled resolving simulations will be illustrated next. This will be conducted in comparison to usually applied simulation methods that cover RANS, hybrid RANS-LES, and LES modeling. All the CES-KOS results presented in this section were obtained on the  $G_2$  grid.

## 4.1. CES-KOS vs. RANS

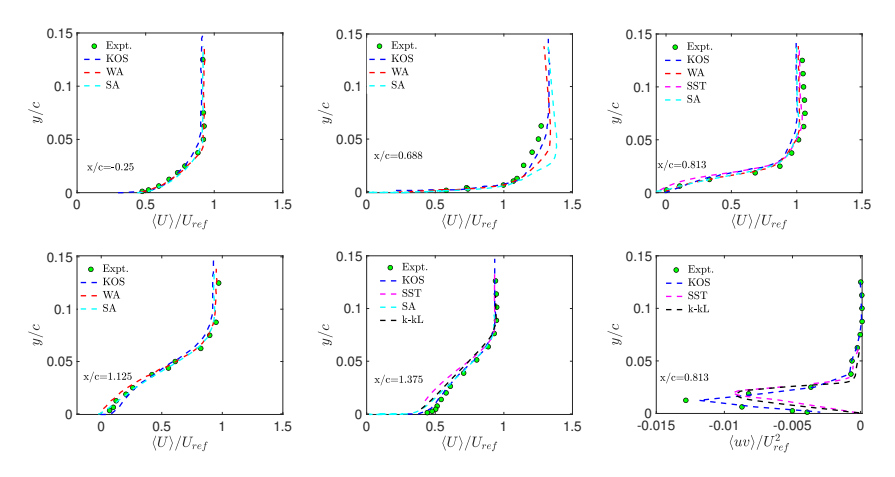
The CES-KOS results were compared with four RANS models, in particular the Wray–Agarwal (WA) model [50], the Spalart–Allmaras (SA) model [50], the shear-stress transport (SST)  $k-\omega$  model [which will be simply referred to as SST model] [51], and the k-kL model [51]. Table 4 reports separation and reattachment locations, bubble length, and % error results from different RANS-type turbulence models. The SST, SA, and k-kL models predict a larger bubble size than given by the experimental data. The WA model had an error of -23.5%, the smallest bubble size, due to late separation. The CES-KOS prediction error is less than 4%. Most RANS models properly predicted the location of separation around x/c=0.70 (with the exception of the WA model). The SST and SA models struggle with an accurate prediction of the reattachment point; they indicate delayed reattachment. The WA and k-kL model predictions are closer to the experiment measurement at 1.10. The best result follows from the CES-KOS simulation with an error of 1.7%.

Table 4. RANS-tv	ne models: Ser	paration and	reattachment	characteristics.

Cases	Grid Points	Separation Location $(x/c)$	Reattachment Location $(x/c)$	Bubble Length $\Delta x/c$	Error in Bubble Length Prediction (%)
Expt. [33]	-	0.70	1.10	0.4	-
CES-KOS	5.4 M	0.703	1.1188	0.4158	3.95
SA [16,50,52]	-	0.688	1.1600	0.472	18
SST-k- $\omega$ [51,53]	0.21 M	0.665	1.1600	0.495	23.7
k-kL [51,54,55]	0.21 M	0.669	1.1200	0.450	12.75
WA [16,50,52]	-	0.817	1.1230	0.306	-23.5

Model comparisons were performed at five axial locations: x/c = -0.25 (initial region), x/c = 0.688 (the region after the shock location but prior to detachment), x/c = (0.813, 1.125) (within the separation zone), and x/c = 1.375 (in the post-reattachment region). Figure 15 shows mean velocity predictions of CES-KOS compared with the predictions of RANS models mentioned above and the experimental results [33]. At x/c = -0.25, all models provide similar predictions of the average velocity profile. Most of the RANS models predict the velocity trend over the bump fairly well except at some locations, in particular within the separation region (x/c = 0.688) where the traditional

SA model clearly overestimates the actual mean velocity profile. CES-KOS matches the experimental data and improves the prediction of SA, WA, SST, and k-kL models in the near shock-wave and post-separation regions. In the post-reattachment region, all predictions are relatively similar, in particular far away from the wall. Close to the wall, SST, SA and CES-KOS models slightly underpredict the measured velocity. Figure 15 also shows a corresponding comparison of Reynolds shear stresses in the post-separation region. The predicted profiles exhibit a qualitative similarity with the experimental data, although the Reynolds stresses are under-predicted. Compared to SST and k-kL turbulence models, the CES-KOS prediction is in much better agreement with the experimental results. In particular, SST and k-kL turbulence models underpredict the shear stress maximum (at about y/c=0.018) by up to 45% for the case considered, whereas the CES-KOS model shows its capability of predicting a shear stress very similar to the experimental results.



**Figure 15.** CES-KOS vs. RANS-type (WA, SA) [50] and (SST, k - kL) [51] models: Profiles of the normalized streamwise velocity  $\langle U \rangle / U_{ref}$  and normalized Reynolds stress  $\langle uv \rangle / U_{ref}^2$  at different axial locations.

Figure 16 shows the time-averaged distributions of surface wall pressure and skin-friction coefficients from RANS models and CES-KOS simulations. The numerical predictions of SA, SST, and k-kL models indicate lower pressure levels in the post-separation region ( $0.7 \le x/c \le 0.938$ ) compared to experimental data. In addition, all RANS models underpredict the surface pressure within the separation region (x/c = 0.938) [possibly due to an inadequate flow resolution and turbulent mixing], whereas CES-KOS marginally overestimates the profile. In the post-separation region, the CES-KOS and SA models exhibit similar skin-friction coefficient profiles. However, after reattachment, the SA simulation fails to capture the secondary  $C_f$  peak at about x/c = 1.2 and the distinct skin-friction distribution in this region, while CES-KOS accurately captures this feature. CES-KOS provides the most accurate skin-friction results compared to the RANS models considered.

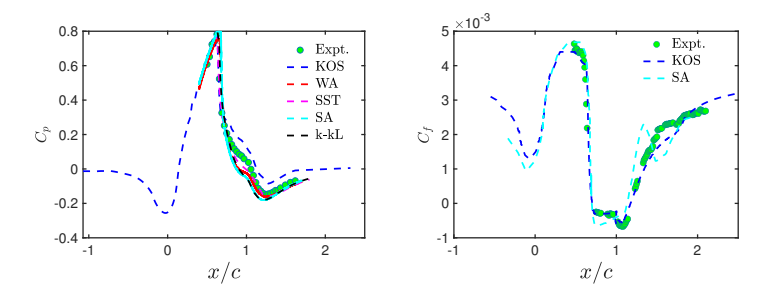


**Figure 16.** CES-KOS vs. RANS-type (WA, SA) [50] and (SST, k - kL) [51] models: Profiles of pressure and skin-friction coefficients.

### 4.2. CES-KOS vs. DES

The inadequacy of RANS to accurately represent unsteady flow characteristics resulted in the development of DES methods. In this subsection, we will compare CES-KOS predictions with three DES methods: the Wray–Agarwal detached eddy simulation (WA-DES) method [50], the Spalart–Allmaras-based DES (SA-DES) [41] method, and the zonal improved delayed DES (IDDES) [34] method. The zonal IDDES technique uses a synthetic turbulence generator at an adaptive RANS-LES interface located at x/c=-0.5 (0.5c upstream of the bump). Due to the different flow regions considered, it is considered as a zonal approach. Table 5 shows characteristic differences in the methods considered in regard to separation and reattachment locations and bubble lengths. IDDES shows early reattachment around x/c=1.08. WA-DES predicts a longer bubble and delayed reattachment at x/c=1.166. The CES-KOS model provides the most accurate predictions.

Table 5. DES-type models: Separation and reattachment characteristics.

Cases	Grid Points	Separation Location (x/c)	Reattachment Location $(x/c)$	Bubble Length $\Delta x/c$	Error in Bubble Length Prediction (%)
Expt. [33] CES-KOS IDDES [34] WA-DES [16,50,52]	5.4M 1.6B	0.70 0.703 0.7 0.696	1.10 1.1188 1.0800 1.1660	0.4000 0.4158 0.3800 0.4700	- 3.95 -5.00 17.50

Figure 17 shows a comparison between velocity profiles provided by DES-based models and the CES-KOS model. The velocity distribution predicted by SA-DES deviates significantly from the empirical data, especially at x/c=0.938 and x/c=1.125. Profiles at other locations also show considerable differences between the model and experiments, indicating SA-DES issues with resolving the thin shear layer. WA-DES results also provide inaccurate results; see the profiles at x/c=0.688 and x/c=1.375. Overall, the CES-KOS model provides the most accurate results.

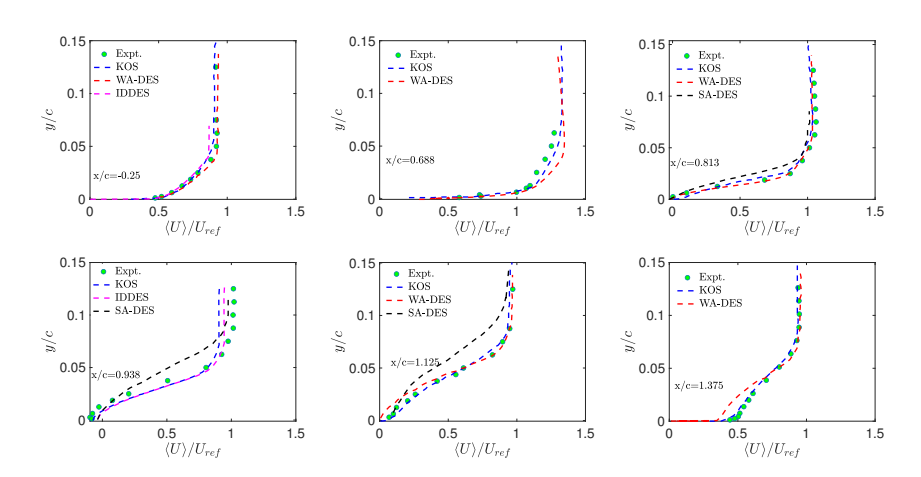


**Figure 17.** CES-KOS vs. DES-type WA-DES, SA-DES [50], and IDDES [34] models: Profiles of the normalized streamwise velocity  $\langle U \rangle / U_{ref}$  at different locations.

Figure 18 shows Reynolds-stress profiles of DES-type models and CES-KOS predictions. We see significant differences, IDDES shows the largest difference of up to 37% compared to experimental data. The Reynolds stress within the separation zone is notably low in IDDES, making it challenging to capture velocity fluctuations. SA-DES and CES-KOS overestimate the stresses off the boundary layer region. Corresponding comparisons of pressure coefficient distributions are shown in the middle of Figure 18. The IDDES results indicate reduced pressure levels in the post-separation region ( $0.85 \le x/c \le 1.2$ ) compared to the experimental data. Notably, IDDES substantially underestimates skin-friction coefficients for 0.12 < x/c < 0.65. Changes in slope in the skin-friction distribution

correlate with longitudinal curvature reversal of the bump's surface at  $x/c \approx 0.12$  and  $x/c \approx 1.1$ . The low pressure values from IDDES correlate with the skin-friction coefficient discrepancies. Specifically, the shear stress reversal predicted by IDDES occurs excessively downstream, consistent with the misplaced shock-wave position.

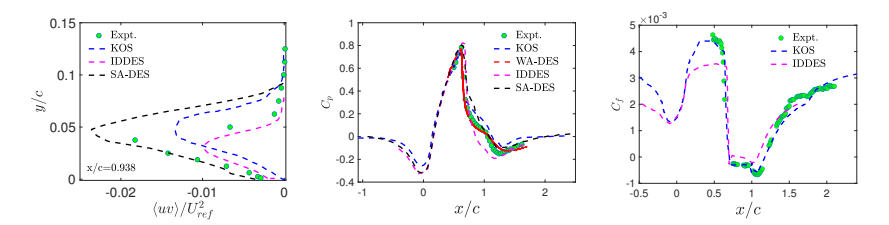


**Figure 18.** CES-KOS vs. DES-type WA-DES, SA-DES [50], and IDDES [34] models: Normalized Reynolds stress  $\langle uv \rangle / U_{ref}^2$ , pressure and skin-friction coefficient distributions.

### 4.3. CES-KOS vs. WMLES and WRLES

Given the notable shortcomings of DES-type models particularly in the attached boundary layer region, as shown above, let us consider next the corresponding comparisons of CES-KOS with WMLES and WRLES. Table 6 shows characteristic differences of the methods considered in regard to separation and reattachment locations and bubble lengths. The reported WMLES misidentifies the reattachment location and overestimates the separation bubble size by up to 17.5%. While WRLES captures the separation point accurately, its predicted bubble length size has a 20% error. In contrast, the CES-KOS model provides the highest accuracy regarding the estimation of the separation length, with an error of only  $\approx$ 4%.

Table 6. LES-type models: separation and reattachment characteristics.

Cases	Grid Points	Separation Location $(x/c)$	Reattachment Location $(x/c)$	Bubble Length $\Delta x/c$	Error in Bubble Length Prediction (%)
Expt. [33] CES-KOS WRLES [42] WMLES [34]	5.4M 24B 24.09M	0.70 0.703 0.69(0.68) 0.7	1.10 1.1188 1.17(1.16) 1.17	0.4000 0.4158 0.48 0.47	3.95 20 17.5

Figure 19 shows in its first row streamwise velocity profiles obtained by CES-KOS, WMLES [41], and WRLES [42]. It may be seen that the CES-KOS model predicts the streamwise velocity more accurately than WMLES and WRLES. In regard to turbulent shear stress profiles shown in the second row, we see a reasonable agreement of WMLES, WRLES, and CES-KOS with experimental data. It is of interest to note that CES-KOS and WRLES provide very similar results. In attached flow regions, WMLES over-predicts the turbulent shear stress (in the same amount as IDDES, as seen above). Due to its delayed reattachment point, WMLES predicts a faster separated shear layer growth and higher maximum Reynolds stresses compared to CES-KOS. These trends have been noted in past numerical studies using alternative models [56,57].

Figure 19 also shows pressure coefficient distributions obtained by CES-KOS, WMLES, and WRLES. The figure helps to illustrate and validate the accuracy of CES-KOS predictions. The CES-KOS and WRLES models accurately predict pressure coefficient profiles due to their sufficient flow resolution ability. In contrast, WMLES predicts a linearly increasing pressure distribution within x/c=(0.7,1.1), which fails to accurately capture the separation zone. Furthermore, both CES-KOS and WRLES show reasonable predictions of the shock location and post-shock pressure recovery. The WRLES results agree slightly better with the experimental data downstream of the bump (between x/c=1.1 and 1.3) compared to the CES-KOS model. Figure 19 also shows skin-friction coefficient distributions obtained by CES-KOS, WMLES, and WRLES. Evidently, WMLES significantly underestimates the skin-friction coefficient in the separation region and fails to accurately represent the post-separation flow physics. The predictions of CES-KOS and WRLES are very similar,

with the exception that CES-KOS better agrees with the experimental data in the  $C_f$  plateau region upstream of separation. Overall, CES-KOS provides the most accurate predictions.

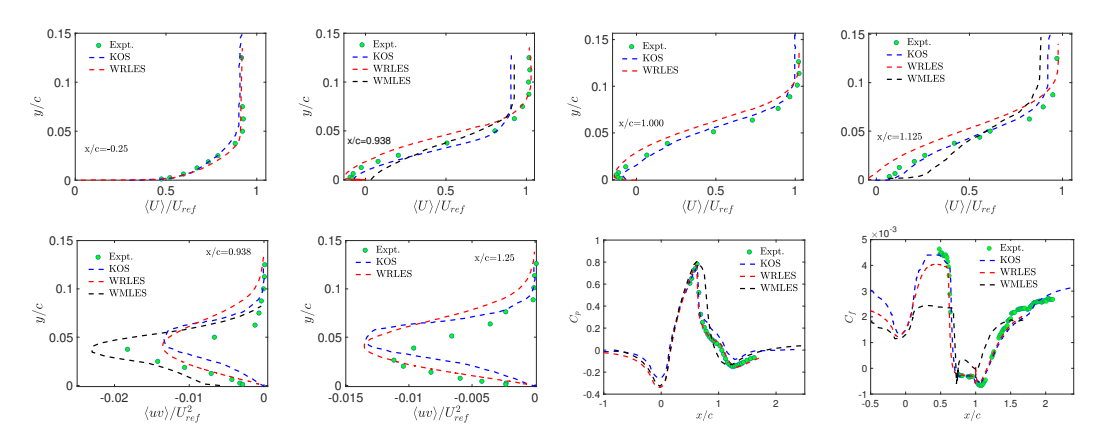


**Figure 19.** CES-KOS vs. LES-type WRLES [42] and WMLES [41] models: Profiles of the normalized streamwise velocity  $\langle U \rangle / U_{ref}$ , Reynolds stress  $\langle uv \rangle / U_{ref}^2$ , pressure, and skin-friction coefficients at different locations.

### 4.4. Cost Estimates

The comparison of computational method features will be completed by an analysis of related computational cost. We follow our previous approach for doing so [25,40]. The simulation cost are specified by

$$C = NN_t = TN/\Delta t. (6)$$

Here, N is the number of grid points applied,  $N_t$  is number of time steps performed,  $T=N_t\Delta t$  refers to the constant total physical simulation time, and  $\Delta t$  (in  $c/U_\infty$ ) is the prescribed simulation time-step. N and  $\Delta t$  are known to vary with Re according to  $N=\alpha_1(Re/Re_0)^{\beta_1}$ ,  $\Delta t=\alpha_2(Re/Re_0)^{-\beta_2}$ , where  $\alpha_1$ ,  $\alpha_2$ ,  $\beta_1$ , and  $\beta_2$  are constants [40]. Here,  $Re_0=2.763M$ , the Reynolds number of the flow considered, is used as normalization, which simplifies the comparisons of computational cost for the flow considered. There is, so far, limited information about the scaling characteristics of computational cost for complex turbulent flows. To make the best possible use of the data we have, we follow our approach presented in Ref. [25]. This means, in regard to WMLES and WRLES, that we apply scalings presented by Yang et al. [58]. In regard to CES-KOS and DES, we use the same scaling assumptions as before [25]. This approach determines the  $\beta_1$  and  $\beta_2$  values shown below. The  $\alpha_1$  and  $\alpha_2$  can be determined by taking reference to simulation settings of the flow considered, which are presented in Table 7 (for the flow considered, we have  $N=\alpha_1$  and  $\Delta t=\alpha_2$ ). The corresponding cost scalings are presented in Table 8, where the range of coarse/fine data in Table 7 is translated into ranges of  $\alpha_1$  and  $\alpha_2$  data in Table 8.

Figure 20 shows the scaling of computational cost: the corresponding minima and maxima of cost per method are defined by the coarse/fine data in Table 7. For simplicity, we approximate the C/T scalings of CES-KOS, WMLES, and DES by  $(Re/Re_0)^{1.1}$  and apply the corresponding fine grid data. Then, the cost of CES to the corresponding cost of WMLES and DES are 1, 9.2, and 296, respectively, independent of Re. The cost ratio of WRLES to CES-KOS is  $77.7 \times 10^3 (Re/Re_0)^{1.62}$ , showing a strong increase with Re. These differences can be attributed to the CES-KOS feature of being derived through the minimization of the hybridization error. A comparison of  $\alpha_3$  values derived here for the finer grid,

$$(\alpha_3^{KOS},\alpha_3^{WRLES},\alpha_3^{WMLES},\alpha_3^{DES}) = (10.8\times10^9,8.39\times10^{14},9.96\times10^{10},32.0\times10^{11}), \tag{7}$$

with corresponding  $\alpha_3$  values determined regarding our previous CES simulations of the NASA wall-mounted hump flow [25] shows a reasonable agreement:

$$(\alpha_3^{KOS}, \alpha_3^{WRLES}, \alpha_3^{WMLES}, \alpha_3^{DES}) = (8.43 \times 10^{10}, 7.28 \times 10^{14}, 1.66 \times 10^{13}, 2.64 \times 10^{11}).$$
 (8)

The latter  $\alpha_3$  values apply to a scaling of  $C/T = \alpha_3 (Re/Re_0)^{\beta_1 + \beta_2}$ . Here,  $Re_0 = 0.936$  M for the NASA wall-mounted hump flow, and  $\beta_1 + \beta_2$  refers to scaling parameters of the method considered.

**Table 7.** Computational cost characteristics of methods.

Factors	CES	-KOS	DES	[34]	WML	ES [41]	WRLI	E <b>S</b> [42]
	Coarse	Fine	Coarse	Fine	Coarse	Fine	Coarse	Fine
$N = \alpha_1$	1.08 M	5.4 M	470 M	1.6 B	20.74 M	24.90 M	3 B	24 B
$\Delta t = \alpha_2$	$1 \times 10^{-3}$	$0.5 \times 10^{-3}$	$1 \times 10^{-3}$	$5 \times 10^{-4}$	-	$2.5 \times 10^{-4}$	$2.86 \times 10^{-5}$	$2.86 \times 10^{-5}$

**Table 8.** Simulation cost estimates (C/T) for WRLES [42,58], WMLES [41,58], DES [21,34,59], and CES-KOS.

Methods	N	$\Delta t$	$C/T = N/\Delta t$	
CES-KOS	$N = \alpha_1 (\frac{Re}{Re_0})^{0.545}$	$\Delta t = \alpha_2 (\frac{Re}{Re_0})^{-0.554}$	$N/\Delta t = \alpha_3 (\frac{Re}{Re_0})^{1.099}$	$\alpha_3 = (1.08 - 10.8) \times 10^9$
WRLES	$N = \alpha_1 (\frac{Re^0}{Re_0})^{1.86}$	$\Delta t = \alpha_2 (\frac{Re^0}{Re_0})^{-0.857}$	$N/\Delta t = \alpha_3 (\frac{R_e^0}{Re_0})^{2.72}$	$\alpha_3 = (1.05 - 8.39) \times 10^{14}$
WMLES	$N = \alpha_1 (\frac{Re^0}{Re_0})^{1.0}$	$\Delta t = \alpha_2 (\frac{Re^0}{Re_0})^{-0.143}$	$N/\Delta t = \alpha_3 (\frac{Re}{Re_0})^{1.143}$	$\alpha_3 = (8.3 - 9.96) \times 10^{10}$
DES	$N = \alpha_1 (\frac{Re^0}{Re_0})^{0.545}$	$\Delta t = \alpha_2 (\frac{R_e^0}{Re_0})^{-0.554}$	$N/\Delta t = \alpha_3 (\frac{Re^0}{Re_0})^{1.099}$	$\alpha_3 = (4.7 - 32.0) \times 10^{11}$

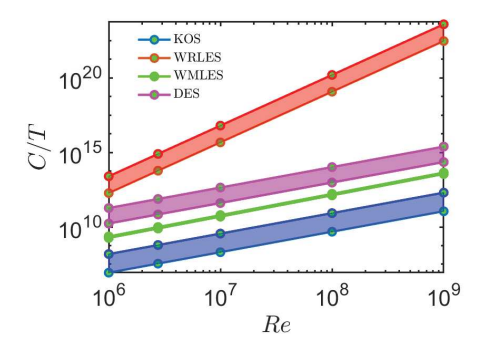


Figure 20. Cost scalings for the methods listed in Table 8.

#### 5. Conclusions

The following conclusions can be drawn in regard to the three objectives O1–O3 considered in the introduction, the simulation performance features, computational cost features, and functionality features of CES in comparison to other simulation methods.

In regard to simulation performance features, the application of typically used RANS as the SST or SA models confirms the known inability of RANS to accurately predict separated turbulent flows, as seen in terms of their bubble length prediction errors of 18-24%. While the corresponding WA model error also corresponds to 24%, the k-kL model performs better, as its bubble length error is only 13%. Velocity profile and pressure coefficient plots indicate that the k-kL model performs relatively similar to the SA model. The SA's model inability to properly represent the structure of the flow considered can be seen in the skin-friction coefficient  $C_f$  plot. Corresponding  $C_f$  plots of the WA model are not reported. In regard to DES methods, IDDES in particular improves the prediction of separation zone characteristics. However, the latter does not guarantee a better overall simulation performance at all, as may be seen in terms of the skin-friction profile obtained by IDDES. Other DES methods as WA-DES and SA-DES suffer from their inability to properly represent the structure of the velocity field. In regard to both WMLES and WRLES, we see predictions of separation bubble characteristics that are relatively similar to RANS predictions (SST and SA predictions). Corresponding skin-friction profile predictions reveal a remarkable inaccuracy of WMLES, and even deficiencies of WRLES. Arguably, the most interesting feature of corresponding CES predictions is a very well-balanced

performance. The CES-KOS considered shows the most accurate prediction of separation bubble characteristics. Velocity, stresses, pressure and skin-friction profiles are in much better agreement with the experimental data than seen in regard to the other methods considered. This applies, in particular, to the use of the  $G_2$  grid. The latter is very coarse compared to grids applied in other methods. However, the use of even coarser grids can reduce the simulation performance, as illustrated in regard to the use of the  $G_1$  grid.

In respect to computational cost features, Figure 20 and computational cost scalings presented in Table 8 speak a clear language regarding the cost differences of methods considered. Using the fine grid data in Table 8 for the flow considered here, the CES costs represent 0.0013, 10.8, 0.34% of the WRLES, WMLES, DES costs, respectively. In regard to our previous CES simulations of the NASA wall-mounted hump flow [25], we found for the flow considered corresponding CES cost ratios of 0.012, 0.51, 31.9% of WRLES, WMLES, DES costs, respectively (see Equation (8). This comparison shows that significant variations in cost ratios can be found, but the CES costs are always much below the costs of other methods. These CES advantages enable the reliable simulations of high Re flows that cannot be properly studied by other methods. This was demonstrated by the simulation of the flow considered at the much higher Re = 5.5 m. The conclusion was that there are very minor *Re* effects, i.e., the flow considered is basically in the asymptotic *Re* regime. The consideration of cost depending on Re is only one way of looking at the question considered. The overall message is that CES opens a new dimension for studying the influence of significant grid refinements to improve predictions via involving a higher fraction of resolved motion.

In respect to functionality features, we see the following. WRLES is constrained by the need to use sufficiently fine grids. Usually, it is not evident at all whether the grids applied enable fully resolved simulations. Hybrid RANS-LES like WMLES methods are known to be seriously affected by simulation settings, the use of different (equilibrium or non-equilibrium) wall models, definitions of regions where different models and grids are applied, different mesh distributions, and set-up options to manage the information exchange between such different flow regions. A similar dependence on simulation settings is found for DES methods: the results depend on the concrete model applied and the definition of differently treated simulation zones. For the same number of grid points, DES and WMLES are known to depend on the mesh organization. An appropriate setting of simulation options requires validation data which are often unavailable. CES methods are independent of such functionality requirements, and the model can be used as is, which is a significant advantage. The CES features enable reliable predictions under conditions where validation data are unavailable.

The present paper on Bachalo–Johnson axisymmetric transonic bump flow simulations continues our previous simulations of periodic hill flows at high *Re* [31] and the NASA wall-mounted hump flow [25]. A natural continuation of this work would be the simulation of even more complex flows, as given by Gaussian bump flows [60]. The latter is outside the scope of this paper. However, corresponding CES simulations appear to be highly promising due to the inherent nature of CES, the incorporation of actual resolved motion, and related stable model response. Such simulations are expected to significantly improve RANS and hybrid RANS-LES as WMLES and DES results. As demonstrated here, it is even plausible to expect improvements of WRLES at a fraction of the computational cost.

**Author Contributions:** Conceptualization, S.H.; Methodology, S.H.; Software, A.F.; Validation, A.F. and S.H.; Formal analysis, A.F.; Investigation, A.F.; Resources, S.H.; Data curation, A.F.; Writing—original draft, A.F.; Writing—review & editing, S.H.; Supervision, S.H.; Project administration, S.H.; Funding acquisition, S.H. All authors have read and agreed to the published version of the manuscript.

Funding: This research received no external funding.

Institutional Review Board Statement: Not applicable.

**Informed Consent Statement:** Not applicable.

**Data Availability Statement:** Data are contained within the article.

Acknowledgments: We are very thankful for computational resources provided by the Advanced Research Computing Center and the Wyoming-NCAR Alliance at the University of Wyoming. Many thanks to A. Kirby for technical support. Financial support of A. Fagbade through the University of Wyoming (College of Engineering and Physical Sciences (CEPS), Dean's Office) is gratefully acknowledged. S. Heinz would like to acknowledge support from the National Science Foundation (AGS, Grant No. 2137351, with N. Anderson as Technical Officer) and support from the Hanse-Wissenschaftskolleg (Delmenhorst, Germany, with M. Kastner as Technical Officer).

Conflicts of Interest: The authors declare no conflict of interest.

#### References

- 1. Runchal, A. (Ed.) 50 Years of CFD in Engineering Sciences; Springer Nature: Singapore, 2020.
- 2. Pope, S.B. *Turbulent Flows*; Cambridge University Press: Cambridge, UK, 2000.
- 3. Sagaut, P. Large Eddy Simulation for Incompressible Flows: An Introduction; Springer: Berlin, Germany, 2002.
- 4. Lesieur, M.; Metais, O.; Comte, P. Large-Eddy Simulations of Turbulence; Cambridge University Press: Cambridge, UK, 2005.
- 5. Piomelli, U. Large-eddy simulation: Achievements and challenges. *Prog. Aerosp. Sci.* 1999, 35, 335–362. [CrossRef]
- 6. Meneveau, C.; Katz, J. Scale-invariance and turbulence models for large-eddy simulation. *Annu. Rev. Fluid Mech.* **2000**, *32*, 1–32. [CrossRef]
- 7. Heinz, S. A review of hybrid RANS-LES methods for turbulent flows: Concepts and applications. *Prog. Aerosp. Sci.* **2020**, 114, 100597. [CrossRef]
- 8. Speziale, C. Turbulence modeling for time-dependent RANS and VLES: A review. AIAA J. 1998, 36, 173–184. [CrossRef]
- 9. Germano, M. Properties of the hybrid RANS/LES filter. Theor. Comput. Fluid Dyn. 2004, 17, 225–231. [CrossRef]
- 10. Hanjalić, K. Will RANS survive LES?: A view of perspectives. ASME J. Fluids Eng. 2005, 127, 831–839. [CrossRef]
- 11. Breuer, A.; Jaffrezic, B.; Arora, K. Hybrid LES-RANS techniques Reynolds-averaged based on a one-equation near-wall model. *Theoretical. Comput. Fluid Dyn.* **2008**, 22, 157–187. [CrossRef]
- 12. Fröhlich, J.; Terzi, D.V. Hybrid LES/RANS methods for the simulation of turbulent flows. *Prog. Aerosp. Sci.* **2008**, 44, 349–377. [CrossRef]
- 13. Mockett, C.; Fuchs, M.; Thiele, F. Progress in DES for wall-modelled LES of complex internal flows. *Comput. Fluids* **2012**, *65*, 44–55. [CrossRef]
- 14. Chaouat, B. The state of the art of hybrid RANS/LES modeling for the simulation of turbulent flows. *Flow Turbul. Combust.* **2017**, 99, 279–327. [CrossRef]
- 15. Menter, F.; Hüppe, A.; Matyushenko, A.; Kolmogorov, D. An overview of hybrid RANS–LES models developed for industrial CFD. *Appl. Sci.* **2021**, *11*, 2459. [CrossRef]
- 16. Spalart, P. Detached-Eddy Simulation. Annu. Rev. Fluid Mech. 2009, 41, 181–202. [CrossRef]
- 17. Shur, M.L.; Spalart, P.R.; Strelets, M.K.; Travin, A. A hybrid RANS-LES approach with delayed-DES and wall-modelled LES capabilities. *Int. J. Heat Fluid Flow* **2008**, *29*, 1638–1649. [CrossRef]
- 18. Spalart, P.R.; Deck, S.; Shur, M.L.; Squires, K.D.; Strelets, M.K.; Travin, A. A new version of detached-eddy simulation, resistant to ambiguous grid densities. *Theor. Comput. Fluid Dyn.* **2006**, *20*, 181–195. [CrossRef]
- 19. Menter, F.R.; Kuntz, M.; Langtry, R. Ten years of industrial experience with SST turbulence model. *Turb. Heat Mass Transf.* **2003**, *4*, 625–632.
- 20. Bose, S.T.; Park, G. Wall-modeled large eddy simulation for complex turbulent flow. *Annu. Rev. Fluid Mech.* **2018**, *50*, 535–561. [CrossRef] [PubMed]
- 21. Larsson, J.; Kawai, S.; Bodart, J.; Bermejo-Moreno, I. Large eddy simulation with modeled wall-stress: Recent progress and future directions. *Mech. Eng. Rev.* **2016**, *3*, 15-00418. [CrossRef]
- 22. Iyer, P.S.; Malik, M.R. Wall-modeled large eddy simulation of flow over a wallmounted hump. In Proceedings of the AIAA Aerospace Sciences Meeting, AIAA SciTech Forum, Washington, DC, USA, 13–17 June 2016; pp. 1–22.
- 23. Wyngaard, J.C. Toward numerical modeling in the "Terra Incognita". J. Atmos. Sci. 2004, 61, 1816–1826. [CrossRef]
- 24. Juliano, T.W.; Kosović, B.; Jiménez, P.A.; Eghdami, M.; Haupt, S.E.; Martilli, A. "Gray Zone" simulations using a three-dimensional planetary boundary layer parameterization in the Weather Research and Forecasting Model. *Mon. Weather Rev.* **2022**, *150*, 1585–1619. [CrossRef]
- 25. Fagbade, A.; Heinz, S. Continuous eddy simulation vs. resolution-imposing simulation methods for turbulent flows. *Fluids* **2024**, 9, 22. [CrossRef]
- 26. Heinz, S. A mathematical solution to the Computational Fluid Dynamics (CFD) dilemma. Mathematics 2023, 11, 3199. [CrossRef]
- 27. Heinz, S. Minimal error partially resolving simulation methods for turbulent flows: A dynamic machine learning approach. *Phys. Fluids* **2022**, *34*, 051705. [CrossRef]
- 28. Heinz, S. From two-equation turbulence models to minimal error resolving simulation methods for complex turbulent flows. *Fluids* **2022**, *7*, 368. [CrossRef]

29. Heinz, S. Remarks on energy partitioning control in the PITM hybrid RANS/LES method for the simulation of turbulent flows. *Flow Turb. Combust.* **2022**, *108*, 927–933. [CrossRef]

- 30. Heinz, S. The continuous eddy simulation capability of velocity and scalar probability density function equations for turbulent flows. *Phys. Fluids* **2021**, *33*, 025107. [CrossRef]
- 31. Heinz, S.; Mokhtarpoor, R.; Stoellinger, M.K. Theory-based Reynolds-Averaged Navier-Stokes equations with large eddy simulation capability for separated turbulent flow simulations. *Phys. Fluids* **2020**, 32, 065102. [CrossRef]
- 32. Heinz, S. The large eddy simulation capability of Reynolds-averaged Navier-Stokes equations: Analytical results. *Phys. Fluids* **2019**, *31*, 021702. [CrossRef]
- 33. Bachalo, W.D.; Johnson, D.A. Transonic, turbulent boundary-layer separation generated on an axisymmetric flow model. *AIAA J.* **1986**, 24, 437–443. [CrossRef]
- 34. Spalart, P.R.; Belyaev, K.V.; Garbaruk, A.V.; Shur, M.L.; Strelets, M.K.; Travin, A.K. Large-eddy and direct numerical simulations of the Bachalo-Johnson flow with shock-induced separation. *Flow Turbul. Combust.* **2017**, *99*, 865–885. [CrossRef]
- 35. Pope, S.B. Ten questions concerning the large-eddy simulation of turbulent flows. New J. Phys. 2004, 6, 35. [CrossRef]
- 36. Heinz, S. Comment on "A dynamic nonlinear subgrid-scale stress model" [Phys. Fluid 17, 035109 (2005)]. *Phys. Fluids* **2005**, 17, 099101. [CrossRef]
- 37. Bredberg, J.; Peng, S.; Davidson, L. An improved k-ω turbulence model applied to recirculating flows. *Int. J. Heat Fluid Flow* **2002**, 23, 731–743. [CrossRef]
- 38. Bredberg, J. On Two-Equation Eddy-Viscosity Models; Department of Thermo and Fluid Dynamics, Chalmers University of Technology: Göteborg, Sweden, 2001.
- 39. Wilcox, D. Turbulence Modeling for CFD, 2nd ed.; DCW Industries: La Canada, CA, USA, 1998.
- 40. Mokhtarpoor, R.; Heinz, S.; Stoellinger, m. Dynamics unified RANS-LES simulations of high Reynolds number separated flows. *Phys. Fluids* **2016**, *28*, 095101. [CrossRef]
- 41. Ren, X.; Su, H.; Yu, H.H.; Yan, Z. Wall-modeled large eddy simulation and detached eddy simulation of wall-mounted separated flow via OpenFOAM. *Aerospace* **2022**, *9*, 759. [CrossRef]
- 42. Uzun, A.; Malik, M.R. Wall-resolved large-eddy simulations of transonic shock-induced flow separation. AIAA J. 2019, 57, 1955–1971. [CrossRef]
- 43. Elkhoury, M. On eddy viscosity transport models with elliptic relaxation. J. Turbul. 2017, 18, 240–259. [CrossRef]
- 44. Lynch, K.P.; Lance, B.; Lee, G.S.; Naughton, J.W.; Miller, N.E.; Barone, M.F.; Beresh, S.J.; Spillers, R.; Soehnel, M. A CFD validation challenge for transonic, shock-induced separated flow: Experimental characterization. In Proceedings of the AIAA Scitech 2020 Forum, Orlando, FL, USA, 6–10 January 2020; pp. 1–19.
- 45. Openfoam Documentation. Technical Report. 2009. Available online: www.openfoam.org (accessed on 1 January 2020).
- 46. Elnahhas, A.; Agrawal, R.; Moin, P. Wall-modeled large-eddy simulation of the Sandia axisymmetric transonic bump. *Cent. Turbul. Res. Annu. Res. Briefs* **2022**, 31–42.
- 47. Mor-Yossef, Y. AUFSR+: Low Mach number enhancement of the AUFSR scheme. Comput. Fluids 2016, 136, 301–311. [CrossRef]
- 48. Gad-el Hak, M.; Bandyopadhyay, P.R. Reynolds number effects in wall-bounded turbulent flows. *Appl. Mech. Rev.* **1994**, 47, 307–365. [CrossRef]
- 49. Örlü, R.; Schlatter, P. On the fluctuating wall-shear stress in zero pressure-gradient turbulent boundary layer flows. *Phys. Fluids* **2011**, 23, 021704. [CrossRef]
- 50. Han, X.; Wray, T.; Agarwal, R.K. Application of a new DES model based on Wray-Agarwal turbulence model for simulation of wall-bounded flows with separation. In Proceedings of the 47th AIAA Fluid Dynamics Conference, Denver, CO, USA, 5–9 June 2017; pp. 1–23.
- 51. Abdol-Hamild, K. Development of kL-based linear, nonlinear, and full Reynolds stress turbulence models, In Proceedings of the AIAA SciTech Forum 2019, San Diego, CA, USA, 7–11 January 2019.
- 52. Wray, T.J.; Agarwal, R.K. A new low Reynolds number one equation turbulence model based on a k- $\omega$  closure. AIAA J. 2015, 53, 2216–2227. [CrossRef]
- 53. Egorov, Y.; Menter, F.; Lechner, R.; Cokljat, D. The scale-adaptive simulation method for unsteady turbulent flow predictions. Part 2: Application to complex flows. *Flow Turbul. Combust.* **2010**, *85*, 139–165. [CrossRef]
- 54. Abdol-Hamid, K.S. Assessments of k-kl turbulence model based on Menter's modification to Rotta's two-equation model. *Int. J. Aerosp. Eng.* **2015**, 2015, 987682. [CrossRef]
- 55. Abdol-Hamid, K.S.; Carlson, J.; Rumsey, C.L. Verification and Validation of the k-kL Turbulence Model in FUN3D and CFL3D Codes. In Proceedings of the 46th AIAA Fluid Dynamics Conference, Washington, DC, USA, 13–17 June 2016.
- 56. Drikakis, D.; Durst, F. Investigation of flux formulae in transonic shock wave: Turbulent boundary layer interaction. *Int. J. Numer. Methods Fluids* **1994**, *18*, 385–413. [CrossRef]
- 57. Sahu, J.; Danberg, J. Navier–Stokes computations of transonic flows with a two-equation turbulence model. AIAA J. 1986, 24, 1744–1751. [CrossRef]
- 58. Yang, X.I.A.; Griffin, K.P. Grid-point and time-step requirements for direct numerical simulation and large-eddy simulation. *Phys. Fluids* **2021**, 33, 015108. [CrossRef]

59. Lei, D.; Yang, H.; Zheng, Y.; Gao, Q.; Jin, X. A modified shielding and rapid transition DDES model for separated flows. *Entropy* **2023**, 25, 613. [CrossRef]

60. Uzun, A.; Malik, M.R. High-fidelity simulation of turbulent flow past Gaussian bump. AIAA J. 2022, 60, 2130–2149. [CrossRef]

**Disclaimer/Publisher's Note:** The statements, opinions and data contained in all publications are solely those of the individual author(s) and contributor(s) and not of MDPI and/or the editor(s). MDPI and/or the editor(s) disclaim responsibility for any injury to people or property resulting from any ideas, methods, instructions or products referred to in the content.